

Pool Boiling Heat Transfer Enhancement with Electrowetting

Aritra Sur¹, Yi Lu¹, Carmen Pascente², Paul Ruchhoeft², Dong Liu¹

¹Department of Mechanical Engineering

²Department of Electrical and Computer Engineering

University of Houston, Houston, Texas 77204-4006, USA

ABSTRACT

Electrowetting (EW) has drawn significant research interests in droplet-based microfluidics, and most applications focus on electronic displays, lab-on-a-chip devices and electro-optical switches, etc. This paper presents a new application of EW in enhancing pool boiling heat transfer. The working approach capitalizes on the complimentary roles of hydrophobicity and hydrophilicity played in boiling and takes advantage of the ability of EW to alter the surface wettability dynamically and reversely. In this work, the effects of alternating current EW (ACEW) on the heat transfer characteristics of various boiling regimes, including the onset of nucleate boiling (ONB), fully developed nucleate boiling, and film boiling at critical heat flux (CHF) conditions, are investigated. A synchronized high-speed optical imaging and infrared (IR) thermography approach is taken to obtain simultaneous measurements of the bubble dynamics and the wall temperature and heat flux distributions on the boiling surface. Based on the experimental data, boiling curves are constructed and the boiling heat transfer coefficients (BHTCs) are computed. Comparisons with the boiling characteristics of the baseline surface without ACEW demonstrate the efficacy of ACEW in enhancing the performance of pool boiling heat transfer. Some insights are also offered to understand the physics of the ACEW-enhanced boiling behaviors.

1. INTRODUCTION

As an effective means of transferring large amount of thermal energy, pool boiling has been employed in various industries involving energy conversion and power generation [1]. The boiling performance is generally characterized by two parameters, the boiling heat transfer coefficient (BHTC) and the critical heat flux (CHF). The BHTC represents the heat removal rate per unit temperature rise in the heated surface, whereas the CHF marks the upper limit of nucleate boiling, beyond which the boiling surface is blanketed with an insulating vapor film and catastrophic burnout may occur. Accordingly, the primary goals of boiling heat transfer enhancement have been to maximize the BHTC and to increase the CHF [2]. Current prevailing approaches are based on chemically or topographically modifying the boiling surface, including

surface roughening [3-7], surface coating [8-19], and fabricating micro/nanoengineered surface structures [20-33], etc. One key premise of these techniques is that the surface wettability can be tailored to affect various aspects of nucleate boiling, such as bubble nucleation [34-38], bubble dynamics [39-44], and CHF [45-49].

Recently, it was realized that, instead of tuning the wettability over the entire surface, introducing localized wetting heterogeneity appears to be a more effective way to augment the boiling performance. This rationale was inspired by the dual role of surface wettability played in boiling, i.e., hydrophobic surface promotes bubble nucleation and increases BHTC, whereas hydrophilic surface is beneficial to CHF enhancement [50, 51]. Consequently, biphilic surfaces with alternating hydrophobic and hydrophilic regions have been manufactured by patterning a hydrophilic surface with hydrophobic materials [41, 51-60] or functionalized nanostructures [61-65]. Significant improvements in both BHTC and CHF were observed on the biphilic composite surfaces, partially due to the increased active nucleation site density, higher bubble growth rate and faster bubble departure frequency as well as the less likelihood of film boiling. Thus, it is concluded that a boiling enhancement surface should consist of a continuous hydrophilic background with distributed hydrophobic spots in order to yield optimized boiling heat transfer characteristics.

While the biphilic surfaces are promising, the main disadvantage is their static and passive nature. Once fabricated, these surface structures and their functionality can no longer be altered. On the other hand, the heat transfer conditions encountered in practical boiling systems, e.g., the boiler in a steam power plant, often fluctuate over time, which may be due to the load-following operations to cope with fluctuating electric demands or the irregularities in the working environment. Under the dynamic conditions, the ability to actively control the boiling characteristics is highly desirable: a hydrophobic surface is maintained at low heat fluxes for the sake of good BHTC, whereas it can be tuned to hydrophilic at high heat fluxes to enhance CHF.

To date, there have been very few studies addressing active, on-demand surface wettability control for boiling heat transfer enhancement. In one approach, ultraviolet (UV)-visible light was employed to induce the hydrophilic-hydrophobic transition on boiling surfaces coated with photosensitive materials, such as TiO_2 [66, 67], carbon nanotubes (CNTs) [68] or organic polymers [69]. Nucleate boiling heat transfer is drastically improved on these light-irradiated surfaces. However, the light irradiation time required to achieve the wettability transition, ranging from 5 minutes to 50 hours, is overly long as compared to a typical boiling ebullition cycle of one to a few seconds. In another study [70], bubble nucleation was manipulated by applying an electric potential to control the adsorption and desorption of charged surfactants on the boiling surface. Adsorption of negatively charged surfactant (sodium dodecyl sulfate) under a positive potential exposes the hydrophobic components of the surfactant to the liquid and renders the surface hydrophobic, thereby promoting nucleation. When the potential is reversed, the surfactant molecules are repelled from the surface, which increases the surface wettability and suppresses nucleation. By combining with individually addressable electrodes, both temporal and spatial control of surfactant boiling was successfully demonstrated.

In this work, an alternative approach for active boiling enhancement, which capitalizes on the ability of electrowetting (EW) to rapidly modulate the surface wettability in a reverse and

robust manner, is presented. With this approach, an inherently hydrophobic boiling surface operates at low-to-moderate heat fluxes, so that the onset of nucleate boiling (ONB) commences spontaneously and excellent BHTC can be obtained. When bubble coalescence intensifies at high heat fluxes, EW effect can be actuated to change the surface to a hydrophilic one within a fraction of a second, thereby keeping the surface rewettable to delay CHF. Furthermore, since alternating current-driven EW (ACEW) is used in the present study, time-harmonic shape oscillations are stimulated at the liquid-vapor interface [71], which can be harnessed to yield favorable bubble dynamics and induce interfacial instability suppress the occurrence of film boiling. To study the ACEW-enhancement of pool boiling heat transfer, experiments are conducted over a wide range of boiling conditions, from ONB, fully developed nucleate boiling to film boiling at CHF, on a hydrophobic surface (as the baseline) and an ACEW-enhanced surface, respectively. A synchronized high-speed optical imaging and IR thermography method is utilized to simultaneously acquire the bubble dynamics and the spatiotemporally resolved wall temperature and heat flux distributions on the boiling surface. The rest of the paper is organized as follows. First, the background of EW is briefly reviewed. Then, the experimental apparatus and the measurement methods are described. Subsequently, the experimental results of pool boiling heat transfer on the two surfaces are presented and compared, and some physical insights are offered to understand the effects of ACEW on various fundamental aspects of pool boiling.

2. ELECTROWETTING

Surface wettability can be altered dynamically by a myriad of external means. For example, light radiation, temperature, magnetic field, electric field and selected solvents have been used to induce the hydrophobic-hydrophilic transition [72-76]. Among them, electrowetting is particularly attractive for its fast response, excellent reversibility, ultralow power consumption and superb robustness [77, 78]. As shown in Fig. 1, a sessile liquid drop resides on a hydrophobic surface with an underneath electrode. The initial contact angle is the intrinsic contact angle, θ_0 . When a voltage signal is applied, the contact angle decreases from θ_0 to a smaller value, θ_a , i.e., the apparent contact angle. The spontaneous spreading of the drop indicates the wettability transition (Fig. 1(c)). The EW-induced contact angle variation can be described by the Lippmann-Young equation

$$\cos \theta_a = \cos \theta_0 + \frac{\epsilon_0 \epsilon_d}{2\sigma_{lv}d} V^2 \quad (1)$$

where V is the applied voltage, ϵ_0 the permittivity of the vacuum, ϵ_d the dielectric constant, d the thickness of the dielectric layer, and σ_{lv} the interfacial tension of the liquid-vapor interface. For a water drop resting on a Teflon-coated surface with silicon dioxide as the dielectric layer ($\theta_0 = 120^\circ$, $\sigma_{lv} = 0.072$ N/m, $\epsilon_d = 3.9$, and $d = 500$ nm), Fig. 2 illustrates that the contact angle decreases from $\theta_0 = 120^\circ$ to $\theta_a = 85^\circ$ when V is increased from 0 V to 35 V. It is noted that θ_a reaches the minimum (80°) at $V \approx 37.5$ V and remains constant irrespective of further increase in V , a phenomenon called the “contact angle saturation”. Nonetheless, Fig. 2 attests that with a moderate voltage signal, the surface wettability can be tuned by EW effectively between the hydrophobic and hydrophilic states. Considering the intimate connection between surface wettability and boiling, Brawlower [79] attempted to enhance pool boiling with direct current

(DC) electrowetting, however, his experimental data showed that, on the contrary, boiling heat transfer is severely deteriorated.

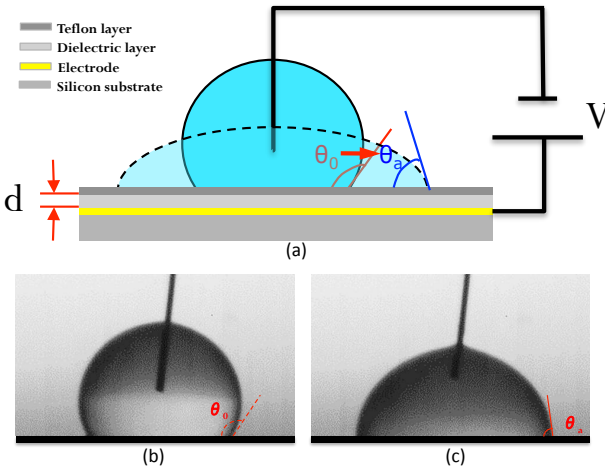


Figure 1. Electrowetting of a water droplet: (a) a typical EW device; (b) the intrinsic hydrophobic state before EW; and (c) the hydrophilic state under EW.

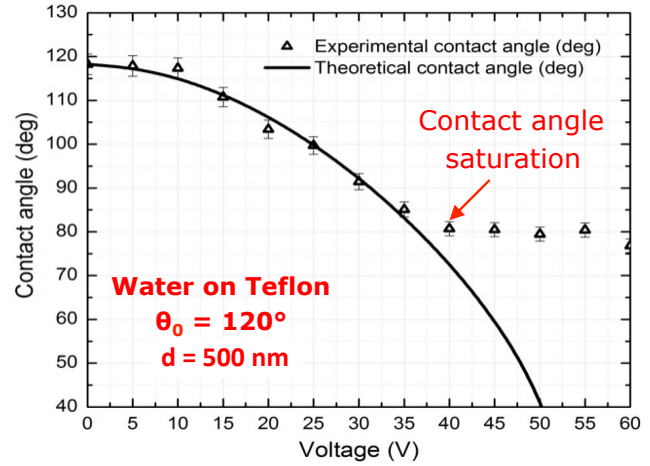


Figure 2. Comparison of the measured contact angle with the prediction from the Lippmann-Young equation.

Fortunately, EW can also be induced by alternating current (AC) voltage signals [80, 81]. In ACEW operation of a liquid drop, a periodic electrical force is exerted on the contact line, which leads to not only the contact line motion but also capillary wave patterns at the liquid-vapor interface [82, 83]. When ACEW is acting on a vapor bubble, similar interfacial oscillations can be stimulated to induce strong streaming flow around the bubble [71, 84]. Hence, it is reasonable to anticipate the streaming flow will favorably reinforce the microconvection as well as the free convection in boiling heat transfer. More importantly, as will be discussed later, ACEW-induced interfacial oscillations have a profound impact on the bubble ebullition process and the instability of film boiling. Consequently, ACEW has the potential to be exploited as a powerful tool to improve BHTC and enhance CHF.

3. EXPERIMENTAL METHODS

3.1. Electrowetting-boiling test device

The EW-boiling test piece is shown in Fig. 3. A 385- μm -thick 3" silicon wafer (Silicon Quest) is used as the substrate, which also functions as the actuating electrode for EW due to the reasonable electrical conductivity of silicon ($1.56 \times 10^{-3} \text{ S/m}$ at 20°C). The wafer has a 500-nm-thick native layer of silicon oxide (SiO_2) thermally grown on both sides. The SiO_2 layer is employed as the dielectric material as SiO_2 has a dielectric constant higher than most fluoropolymers that are commonly used in EW studies. A thin layer (70 nm) of Teflon (AF2400, Dupont) is spin-coated on the wafer to generate the hydrophobicity. To improve the affiliation of Teflon to SiO_2 , a silane-based adhesion promoter (FSM-660-4, Cytonix) is dip-coated on the surface before spin-coating Teflon. On the other side of the silicon wafer, a chromium (Cr) thin-film heater (20 mm long \times 20 mm wide \times 200 nm thick) is fabricated in the center region, as

indicated in Fig. 3. Electrical connections to the external circuits are fabricated using copper (Cu). The heater circuit is electrically separated from the EW circuit by the SiO₂ layer.

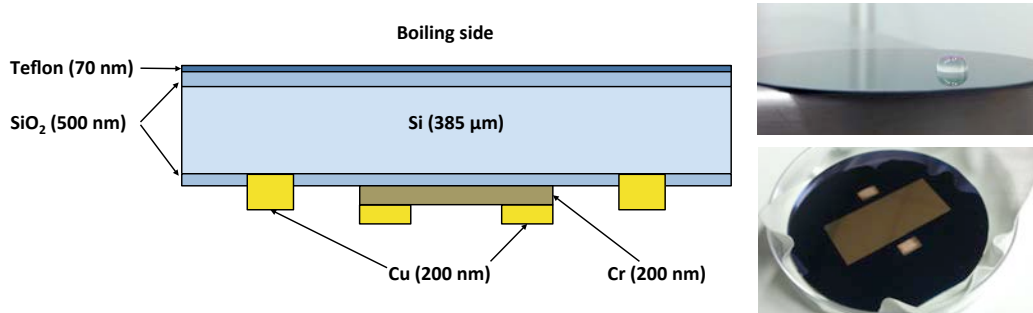


Figure 3. Test device for ACEW-enhanced pool boiling heat transfer experiments.

Figures 4(a) and (b) show the AFM images of the bare SiO₂ surface and the Teflon-coated surface, whereas Fig. 4(c) depicts the latter surface after a few cycles of boiling experiments. The average surface roughness is measured to be 0.165 nm, 1.12 nm and 6.95 nm, respectively, for the three surfaces. Thus, the boiling process does not drastically change the surface morphology. Throughout the experiments, the boiling surface can be considered as a smooth one without any microstructures that may trap vapor/gas and act as nucleation sites for bubble incipience.

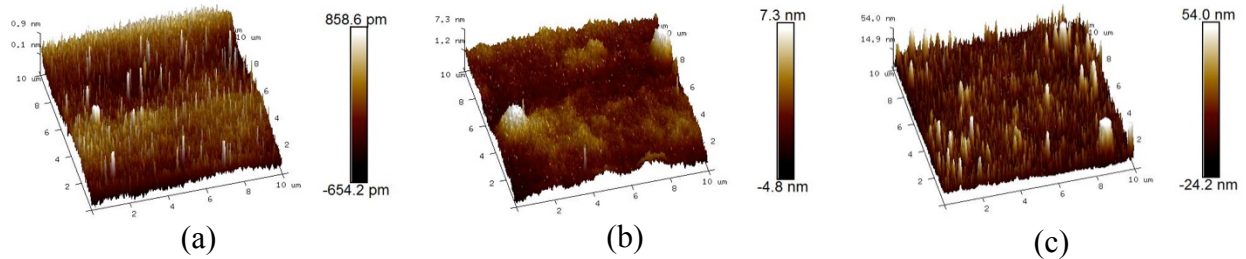


Figure 4. AFM images of (a) a bare SiO₂ surface, (b) a Teflon-coated surface before boiling, and (c) a Teflon-coated surface after boiling (without reaching the CHF conditions).

3.2. Experimental apparatus

Figure 5(a) depicts the apparatus constructed for the boiling heat transfer experiments. The boiling chamber is made of aluminum alloy and has a total volume of 4.5 L. It houses a G-10 fixture to hold the EW-boiling test device as well as four immersion cartridge heaters (HT 20873, Thermal Solutions) in place. The EW-boiling test piece sits on the top of the G-10 fixture, and the electrical wires are connected through two access ports from the bottom (Fig. 5(b)). A through hole is opened at the center of the fixture to facilitate the IR imaging from the backside of the test piece. The cartridge heaters are used to degas the liquid before the experiments and to maintain the saturated boiling condition during the experiments. The bulk liquid temperature is monitored by a thermocouple inserted in the liquid pool in the chamber. A reflux condenser is fitted to the top of the chamber to condense the vapor generated during the

boiling experiments, thereby reclaiming the liquid volume. One end of the reflux condenser is open to the ambient to ensure that the experiments are conducted at atmospheric pressure. Four glass windows are installed on the sides of the chamber to provide optical path for high-speed imaging of the bubble behaviors. The boiling chamber is set up on a custom-built test rig, which also accommodates both the high-speed optical camera and the IR camera.

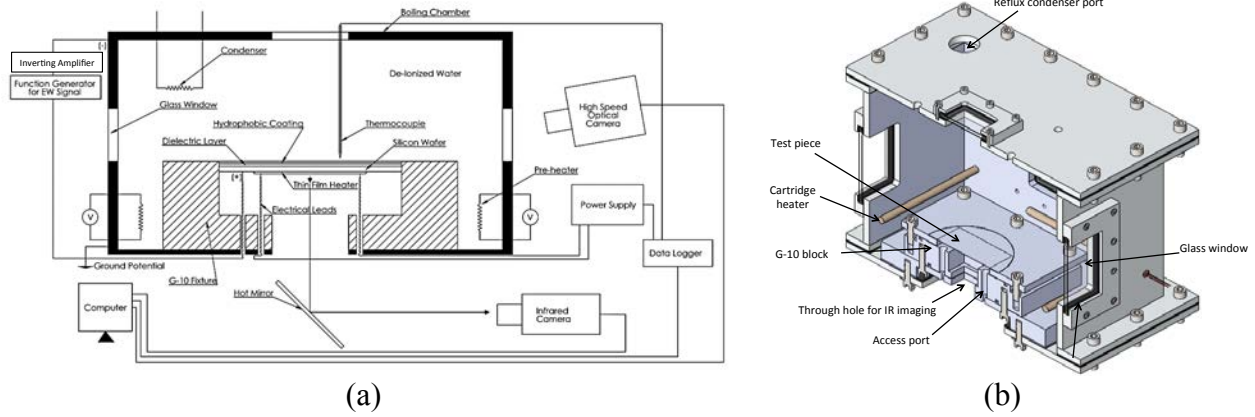


Figure 5. Apparatus for the pool boiling heat transfer experiments.

The thin-film heater on the EW-boiling device is powered by a DC power supply (N5771A, Agilent). The current flowing through the heater, I , is obtained with the help of a shunt resistor, and the voltage drop across the heater, U , is measured by the four-probe method. The cartridge heaters are regulated by two variacs (1010B, ISE). The measured ambient temperature, bulk liquid temperature and the power supplied to the thin-film heater are recorded by a data acquisition system (34970A, Agilent).

In EW-enhanced boiling experiments, the actuating EW signals are produced by an arbitrary waveform generator (Fluke 294-U, Fluke) in combination with an inverting amplifier (BOP 200-1D-BIT 4886, KEPCO). The AC actuation signal is a 50% duty cycle square pulse wave with an amplitude of V_0 , as shown schematically in Fig. 6. The root mean square (RMS) value of the voltage, V_{RMS} , is calculated as

$$V_{RMS} = V_0 / \sqrt{2} \quad (2)$$

This waveform is carefully selected over other waveforms, such as sinusoidal or sawtooth waves, in order to maximize the strength of the electrical force during the *on* cycle, which is proportional to V_{RMS}^2 [83]. For instance, if sinusoidal signal is used, the electrical force will decay from its maxima once the signal passes the peak and valley points. In contrast, a constant electrowetting force can be maintained during the *on* cycle of 50% duty cycle square pulse signal. Additionally, it has been observed [85] that pool boiling depends strongly on the signal frequency, and optimal boiling heat transfer can be achieved at specific frequencies for different boiling regimes. However, since the primary goal of this work is to establish the overall efficacy of EW enhancement, the frequency-dependent boiling heat transfer characteristics is the subject of a future publication, and will not be discussed in this paper. For the results reported here, EW

is actuated with a fixed V_{RMS} ($= 78$ V) and a constant frequency ($f = 10$ Hz). It is noted that V_{RMS} exceeds the saturation voltage (35 V) shown in Fig. 2 (which was obtained for a water drop residing in a gaseous environment) as the EW motion of bubbles involves displacing the surrounding liquid, thus requiring higher voltage to operate.

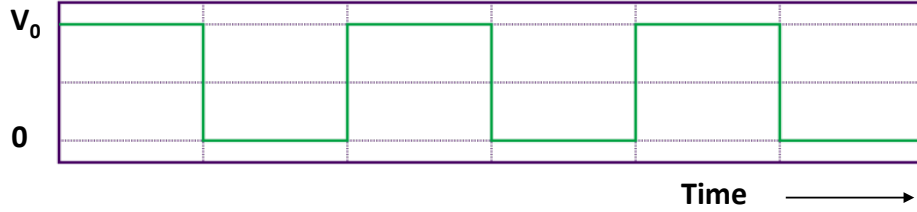


Figure 6. Schematic representation of the applied ACEW signal.

3.3. Measurement techniques

A synchronized optical imaging and IR thermography approach is adopted to obtain simultaneous measurements of the bubble dynamics and the wall temperature distribution during boiling [86]. The bubble ebullition process, including nucleation, growth and departure, is visualized by a high-speed camera (Fastcam-Ultima APX, Photron). The frame rate is varied from 1000 – 8000 frames per second (fps), and the shutter speed is set to 1/16000 s. A high-power illumination source is used to compensate for the short exposure time at high frame rates. A Nikon micro-lens (f 2.8) is used to resolve the details of the individual bubbles in nucleate boiling regime, and a Nikon 18-105 mm lens (f 3-5.6) is employed to observe the boiling characteristics near/at CHF where discrete bubbles can no longer be discerned.

The instantaneous temperature distribution at the surface of the thin-film heater is acquired by an IR camera (SC 7650, FLIR). The IR camera has an Indium Antimonide (InSb) sensor array that operates in the midwave IR range ($3 - 5 \mu\text{m}$) and measures over a temperature range of $5 - 300^\circ\text{C}$. The maximum resolution is 640×512 pixels with a spatial resolution of $150 \mu\text{m}/\text{pixel}$. The maximum frame rate used in this work is 180 Hz. The IR camera is calibrated using a blackbody source (BB 702, Omega). To facilitate the IR measurement, a water-based black paint is sprayed on the heater surface with a thickness of about $6 \mu\text{m}$, which yields an emissivity of $\varepsilon_h \sim 0.97$. A gold-coated hot mirror (N-BK7, Edmund Optics) is used to re-direct the thermal radiation from the heater to the IR camera, as shown in Fig. 7(a). The hot mirror is highly reflective to IR irradiation with a reflectance $\rho_m = 0.98$. The raw image acquired by the IR camera is a two-dimensional (2D) infrared intensity distribution as shown in Fig. 7(b), which is then converted to the temperature scales by a built-in factory calibration.

A pulse generator (BNC 565, Berkeley Nucleonics) is used to synchronize the optical and IR cameras so that information of the bubble ebullition, the temperature field and the heat flux distribution can be correlated in the data analysis.

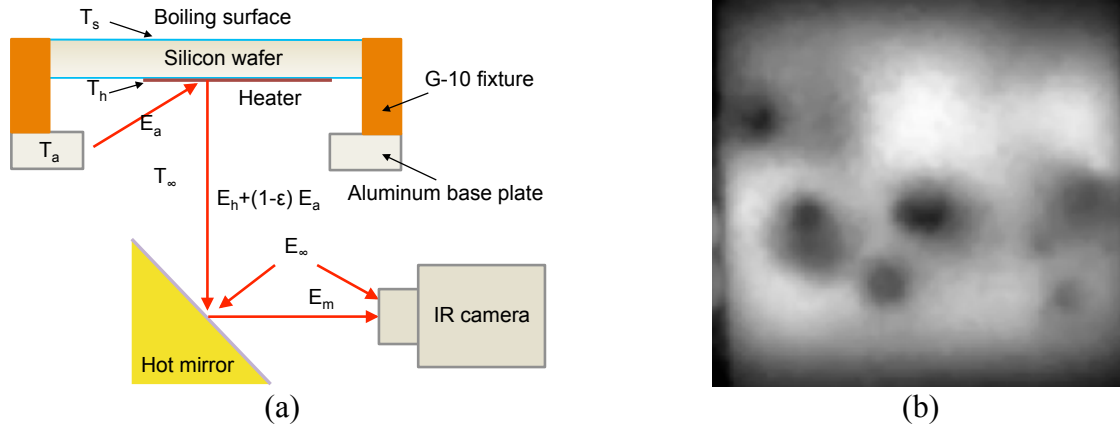


Figure 7. (a) Schematic of the IR temperature measurement and the associated thermal energy transport pathways, and (b) a raw image acquired from the IR camera.

3.4. Test procedures

Prior to each experiment, deionized (DI) water in the boiling chamber is degassed by vigorously boiling for three hours with the cartridge heaters. Afterwards, the power level to the cartridge heaters is lowered to be just enough to maintain the bulk liquid at the saturation temperature. Subsequently, the pool boiling heat transfer experiments are conducted by slowly increasing the power input to the thin-film heater on the EW-boiling test piece. Once the power level is set, it usually takes 10 – 15 minutes for the system to stabilize. A steady state is deemed to have reached when the average surface temperature measured over a representative region of interest (ROI) becomes stable and remains so for at least 5 minutes (Note: the instantaneous fluctuations depend on the specific boiling regime). Then, the video streams of synchronized optical and IR images are collected by the computer. The other measured parameters, including the bulk fluid temperature, the ambient temperature and the applied voltage and current, are recorded by the data acquisition system. Following that, the power input is increased gradually with small increments until the CHF condition is reached. In this work, the CHF condition is determined by the abrupt rise in the boiling surface temperature.

To highlight the effects of ACEW on boiling heat transfer, the experiments are conducted using the EW-boiling test piece in two different cases. Case I represents the baseline case in which no ACEW signals are applied and boiling occurs on the hydrophobic surface. In Case II, an AC signal ($f = 10$ Hz and $V_{RMS} = 78$ V) is used to actuate ACEW during the entire course of the boiling process.

3.5. Data deduction and uncertainty analysis

3.5.1. IR temperature measurement

The heater surface temperature is measured by the IR thermography. As shown in Fig. 7(a), a few sources contribute to the thermal radiation directly received by the IR sensors. Thus, the apparent temperature registered by the IR camera, T_{IR} , must be corrected to reflect the true

heater surface temperature, T_h . After considering various contributing factors, the following expression is derived for T_h [85]

$$T_h = \left\{ \left[\frac{\alpha_s(T_{IR}^4 - T_s^4) - (1 - \tau_\infty)T_\infty^4}{(1 - \varepsilon_m)\tau_\infty} - (1 - \varepsilon_h)T_a^4 - (1 - \tau_\infty)T_\infty^4 \right] / \varepsilon_h \right\}^{0.25} \quad (3)$$

where T_s is the temperature of the Sterling-cooled sensor array of the IR camera ($= 77$ K), T_∞ and T_a are the ambient temperature and the average temperature of the test fixture, respectively; α_s is the absorptance of the sensor (~ 1) [87, 88], and τ_∞ is the transmittance of air ($= 0.98$) [89]. Note that this correction is applied to the temperature measured by each every pixel in the ROI.

3.5.2. Wall temperature of boiling surface

Construction of the boiling curves requires information of the average wall heat flux and the average wall temperature of the boiling surface. Since the surface area ratio of the heater to the silicon wafer is small ($\sim 2\%$) and the wafer is very thin, the thermal spreading resistance is so high that it is reasonable to assume the heat generated by the thin-film heater is only conducted to a region of the same area on the other side of the wafer [90, 91]. Thus the average wall heat flux on the boiling surface can be estimated from the power input to the heater

$$q_h'' = \frac{U \times I}{A_h} \quad (4)$$

where U and I are the voltage drop across and the current flow through the heater, and A_h is the heater surface area. Heat losses from the heater to the ambient via natural convection and radiation are found to be negligible ($< 1\%$) [85].

The wall temperature of the boiling surface, T_w , at each pixel is deduced from T_h , after taking into account the heat conduction effect

$$T_w = T_h - q_h'' t_{Si} / k_{Si} \quad (5)$$

where t_{Si} is the thickness of the silicon wafer ($t_{Si} = 385 \mu m$) and k_{Si} is the thermal conductivity of silicon ($k_{Si} = 148 W/mK$). For any given heat flux, multiple instantaneous measurements of T_w in the ROI are obtained over at a time scale that is suitable for the corresponding boiling regime, and the area average, $\overline{T_{w,i}}$, is calculated for each measurement ($i = 1, \dots, n$, where n is the number of instantaneous measurements). Subsequently, the average wall temperature of the boiling surface, $\overline{T_w}$, is taken as the mean of these average values

$$\overline{T_w} = \frac{1}{n} \sum_{i=1}^n \overline{T_{w,i}} \quad (6)$$

3.5.3. Local wall heat flux

In the present work, only the heater surface temperature, T_h , is readily known from the experimental measurements. Strictly speaking, an inverse heat conduction problem (IHCP) needs to be solved in order to acquire the local wall heat flux distribution, q_b'' [92-95]. However, past studies show that the solution of IHCPs is mathematically involved and is sensitive to errors

in the temperature measurements. Therefore, an energy balance-based model is used in this work to estimate q_b'' for its simplicity and robustness [92].

Figure 8 shows a volume element of the silicon substrate with the transverse dimensions corresponding to a pixel on the IR image ($\Delta x = \Delta y = 150 \mu\text{m}$) and the z-directional dimension being the thickness of the silicon wafer ($t_{Si} = 385 \mu\text{m}$). Applying energy conservation yields

$$q_x + q_y + q_h - q_{x+\Delta x} - q_{y+\Delta y} - q_b = \rho C_p \frac{\partial T}{\partial t} (\Delta x \Delta y \cdot t_{Si}) \quad (7)$$

where q_x , q_y , and q_h represent the heat transfer rate entering the pixel element in the x , y and z directions, $q_{x+\Delta x}$, $q_{y+\Delta y}$, and q_b are the heat transfer rate leaving the element, and $\rho C_p \frac{\partial T}{\partial t} t_{Si} \Delta x \Delta y$ is the rate of energy accumulation in the element. In the above, the input heat transfer is $q_h = q_h'' \Delta x \Delta y$, and the boiling heat transfer at the boiling surface is $q_b = q_b'' \Delta x \Delta y$.

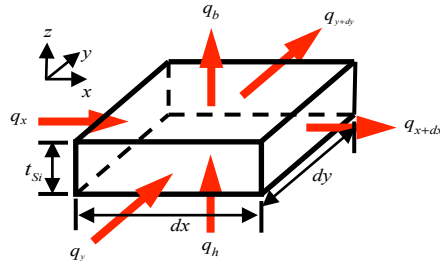


Figure 8. Differential unit volume used for the computation of local wall heat flux.

Using Taylor series expansion and neglecting the higher order terms, Eq. (7) transforms to

$$-\frac{\partial q_x}{\partial x} \Delta x - \frac{\partial q_y}{\partial y} \Delta y + q_h - q_b = \rho C_p \frac{\partial T}{\partial t} t_{Si} \Delta x \Delta y \quad (8)$$

Since $q_x = -k_{Si} \frac{\partial T}{\partial x} t_{Si} \Delta y$ and $q_y = -k_{Si} \frac{\partial T}{\partial y} t_{Si} \Delta x$, Eq. (8) is further reduced to

$$k \left(\frac{\partial^2 T}{\partial x^2} + \frac{\partial^2 T}{\partial y^2} \right) + \frac{(q_h - q_b)/t_{Si}}{\Delta x \Delta y} = \rho C_p \frac{\partial T}{\partial t} \quad (9)$$

Accordingly, the heat flux at the boiling surface is obtained as

$$q_b'' = \left[k \left(\frac{\partial^2 T}{\partial x^2} + \frac{\partial^2 T}{\partial y^2} \right) - \rho C_p \frac{\partial T}{\partial t} \right] t_{Si} + q_h'' \quad (10)$$

In this 2D model, a key assumption is that there is no z-directional temperature variation. This can be justified from two aspects: 1) the thickness of the silicon wafer is at least one order of magnitude smaller than the distance through which a thermal wave would penetrate before decaying to 90% of its initial amplitude [85, 96]. In other words, any change in the heater surface temperature, T_h , will lead to an instantaneous change in the boiling surface temperature, T_w , on the other side of the wafer; and 2) Even at the maximum input heat flux ($q_h'' = 142.6$

kW/m²), the corresponding temperature difference across the thickness will not exceed $\Delta T = T_h - T_w = q_h'' t_{Si} / k_{Si} = 0.37^\circ\text{C}$, a value that is smaller than the uncertainty of the temperature measurement.

In order to assess q_b'' , the spatial and temporal derivatives of the temperature field, $\partial^2 T / \partial x^2$, $\partial^2 T / \partial y^2$ and $\partial T / \partial t$, must be evaluated. Following the argument of a 2D temperature profile, the measured heater surface temperature, T_h , is used in the calculation. The discretization of the spatial terms at the location (x, y) is based on a central differencing scheme of a second order accuracy

$$\frac{\partial^2 T}{\partial x^2} = \frac{T_{x+\Delta x, y} - 2T_{x, y} + T_{x-\Delta x, y}}{(\Delta x)^2} \quad (11)$$

$$\frac{\partial^2 T}{\partial y^2} = \frac{T_{x, y+\Delta y} - 2T_{x, y} + T_{x, y-\Delta y}}{(\Delta y)^2} \quad (12)$$

The temporal term is obtained from the two consecutive IR temperature measurements taken at the same location using a forward Euler discretization scheme

$$\frac{\partial T}{\partial t} = \frac{T_{t+\Delta t} - T_t}{\Delta t} \quad (13)$$

where Δt is the time lapse between two consecutive IR images.

3.5.4. Boiling heat transfer coefficient

The average boiling heat transfer coefficient (BHTC) is defined as

$$h = q_h'' / (\overline{T_w} - T_{sat}) = q_h'' / \Delta T_{sup} \quad (14)$$

where T_{sat} is the saturation temperature of water at atmospheric pressure, and ΔT_{sup} the wall superheat ($\Delta T_{sup} = \overline{T_w} - T_{sat}$).

3.5.5. Uncertainty analysis

An uncertainty analysis is performed using the Kline-McClintok approach [97], which reveals the uncertainty in the temperature measurement is $\pm 1^\circ\text{C}$, and the uncertainty in the heat flux measurement is less than 1% [85].

4. RESULTS AND DISCUSSION

In this section, the experimental results are presented in the order of the following boiling regimes, ONB, fully developed nucleate boiling and film boiling. Whenever possible, data from the baseline experiments (Case I) are compared with the EW-enhanced boiling (Case II). It is worth noting that the goal of this study is not to attain the best boiling heat transfer performance or the maximum CHF, but, rather, to demonstrate a new venue to enhance pool boiling by tuning surface wettability with ACEW.

4.1. ONB

When there is no ACEW, ONB occurs at $q_h'' = 3.7 \text{ kW/m}^2$ on the hydrophobic surface (Case I). Figure 9(a) shows that as the bubble grows after nucleation ($t = 0 \text{ ms}$), its contact radius on the wall, i.e., the bubble footprint, expands quickly ($t = 101.5 \text{ ms} - 1.472 \text{ s}$). Evidently, the contact angle remains obtuse at the three-phase contact line throughout the growing process. Starting from $t = 1.320 \text{ s}$, the bubble shape changes from convex to partially concave near its root on the wall, due to the uplifting buoyancy forces. Subsequently, a neck is formed which connects the upper portion of the bubble to its base ($t = 1.517 \text{ s}$). As the bubble height continues to increase, the neck region gradually diminishes till it is pinched completely at $t = 1.523 \text{ s}$, signifying the bubble departure. The detaching bubble leaves a tiny vapor patch behind it that will serve as the nucleus to initiate the next ebullition cycle. The entire nucleation, growth and departure process lasts for 1.523 s , corresponding to a departure frequency of 0.66 Hz .

Figure 9(b) illustrates the bubble ebullition when ACEW signal is actuated (Case II). As compared to Case I, two major distinctions can be observed. First, the bubble departure occurs much earlier (at $t = 282.75 \text{ ms}$) and the ebullition frequency increases to 3.5 Hz (about 5 times that in Case I). Second, no vapor residual is found in the wake of the departing bubble. The observed bubble behaviors can be attributed to the modulated bubble dynamics by ACEW. A quantitative analysis of the images [85] reveals the maximum size of the bubble footprint in Fig. 9(b) is only one half of that in Fig. 9(a), due to the fact that the electrical force is retarding the contact line spreading on the wall. Consequently, electrowetting assists buoyancy in competing with the surface tension forces, which hold the bubble on the wall and whose magnitude is proportional to the perimeter of the bubble footprint, to trigger premature departure of the bubble. Moreover, ACEW-stimulated interfacial oscillations induce appreciable streaming flow in the proximate fluid, which helps destabilize the bubble and accelerate its removal [71, 85]. Another observation is that the incipience heat flux increases to $q_h'' = 7.5 \text{ kW/m}^2$ when the ACEW effect is present. This is because the improved surface wettability imposes a higher energy barrier that must be overcome for nucleation to take place [1]. In addition, if a bubble ever nucleates, the ACEW-induced streaming flow augments natural convection in its surrounding, making the thermal conditions less favorable for the nascent bubble [85]. Hence, a higher incipience heat flux is necessary to sustain stable ONB.

The local wall temperature at a single nucleation site is measured by IR thermography, and the average value is calculated over the area covered by the maximum footprint of the bubble. The time history of the local average wall temperature is shown in Fig. 10. The bubble ebullition cycles can be identified from the peak-valley variations, which reveal the corresponding periods are similar to those observed in Fig. 9(a) ($1.2 - 1.5 \text{ s}$ for Case I) and Fig. 9(b) ($0.3 - 0.5 \text{ s}$ for Case II). Overall, the local average wall temperature fluctuates between 101.7°C and 102.1°C on the hydrophobic surface, whereas the range drops to $100.6 - 101.6^\circ\text{C}$ under ACEW even though the heat flux is increased from $q_h'' = 3.7 \text{ kW/m}^2$ to $q_h'' = 7.5 \text{ kW/m}^2$. It is postulated that both the accelerated bubble departure and the ACEW-induced streaming flow contribute to the enhanced boiling heat transfer.

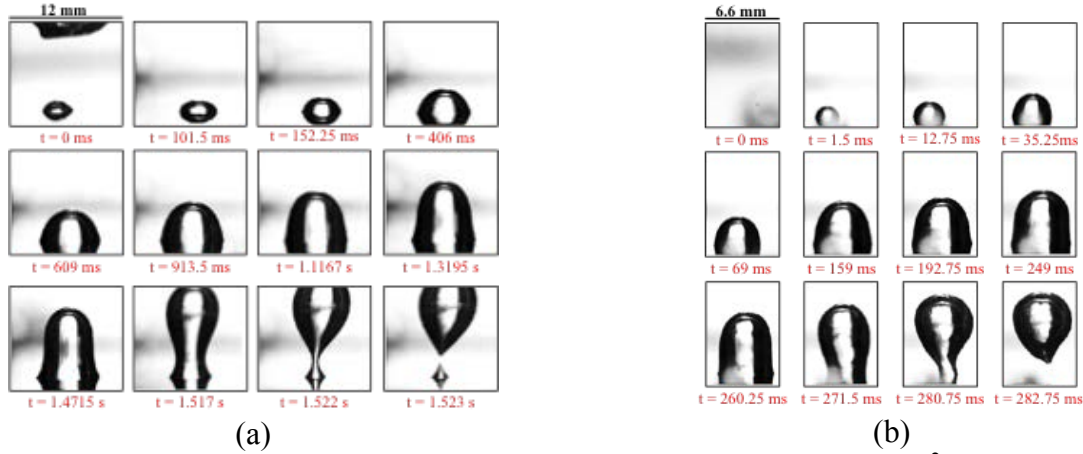


Figure 9. Bubble ebullition at ONB in: (a) Case I: no ACEW, $q_h'' = 3.7$ kW/m² and (b) Case II: ACEW-enhanced boiling, $q_h'' = 7.5$ kW/m² ($V_{RMS} = 78$ V, $f = 10$ Hz).

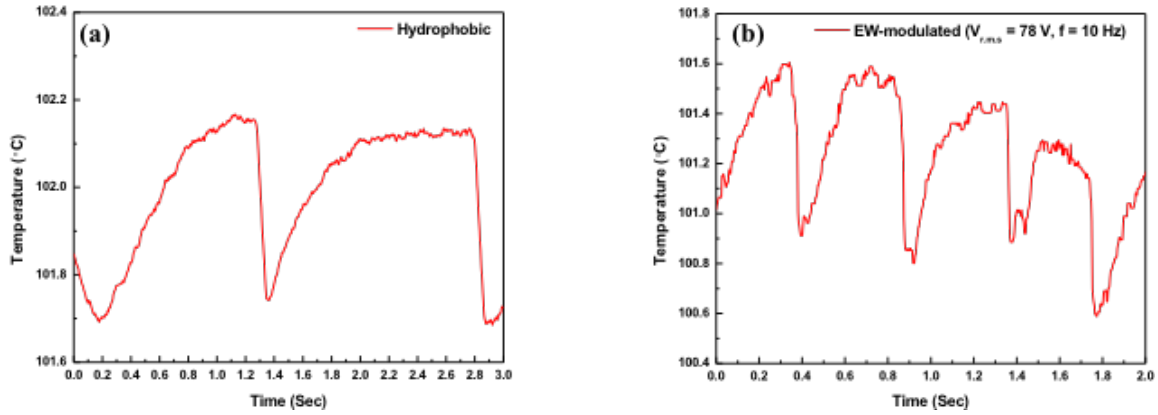


Figure 10. Variation of the local average wall temperature at a nucleation site at ONB: (a) Case I: no ACEW, $q_h'' = 3.7$ kW/m² and (b) Case II: ACEW-enhanced boiling, $q_h'' = 7.5$ kW/m² ($V_{RMS} = 78$ V, $f = 10$ Hz).

4.2. Fully developed nucleate boiling

As the applied heat flux increases, more and more nucleation sites are activated and the bubble ebullition frequency rises at each site. When vapor generation becomes so intensive that the neighboring bubbles start to coalesce during the last stages of growth and departure, boiling enters the fully developed nucleate boiling regime. At $q_h'' = 62.6$ kW/m² on the hydrophobic surface (Case I), fully developed nucleate boiling is featured by rapid bubble merger and even formation of vapor slugs and columns. Figure 11(a) shows two bubbles (marked by red arrows) that are initially isolated at $t = 0$ ms agglomerate into a larger-sized bubble at $t = 17.5$ ms. The merging process continues until the new bubble (marked by a black arrow) takes off at $t = 70$ ms. By contrast, when ACEW is actuated at the same heat flux level, numerous small bubbles are generated but they keep apart from each other without observable agglomeration (Fig. 11(b)). The subsequent growth and departure of these bubbles resemble that in Fig. 9 at the ONB

conditions. The suppressed bubble coalescence can be attributed to the effect of EW on bubble dynamics, such as the restrained contact line spreading and the premature bubble departure.

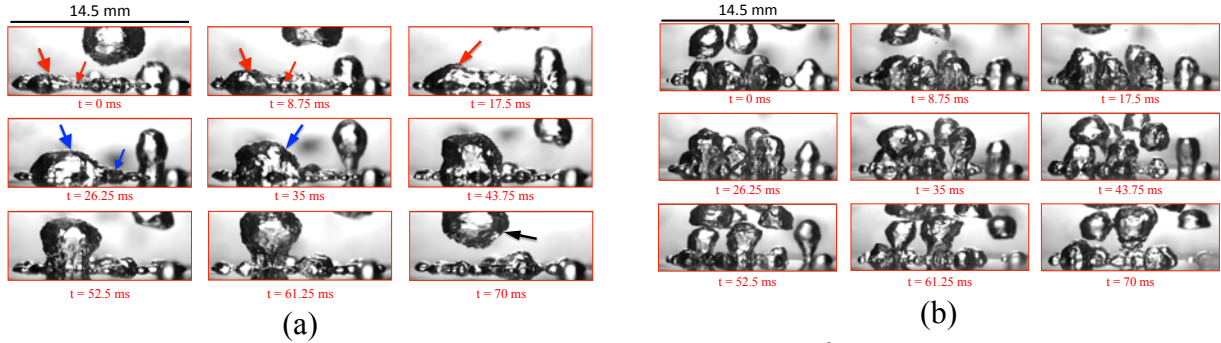


Figure 11. Fully developed nucleate boiling at $q''_h = 62.6 \text{ kW/m}^2$ in: (a) Case I, no ACEW and (b) Case II: ACEW-enhanced boiling ($V_{RMS} = 78 \text{ V}$, $f = 10 \text{ Hz}$).

The impact of EW on fully developed nucleate boiling is further examined from the spatiotemporally resolved wall temperature measurements (shown in Fig. 12). In each frame, the light-colored areas (orange to red) signify hot spots with $T_w > 108^\circ\text{C}$, which are the dryout regions covered by the vapor bubbles. The dark-colored (blue) areas represent the regions in contact with the bulk liquid ($T_w \leq 103^\circ\text{C}$). Since the IR camera is synchronized with the high-speed camera, the measured temperature field can be correlated with the optical visualization of the bubble ebullition events depicted in Fig. 11. For instance, the bubble coalescence in Fig. 11(a) can be clearly tracked from the fusing process of two adjacent hot spots in Fig. 12(a). When ACEW is present (Fig. 12(b)), only some smaller hot spots reside sporadically on the wall, indicating a lesser degree of bubble coalescence. Even when the coalescence does occur, the bubble footprint remains by and large confined on the surface without further growth, which is consistent with the observations in Fig. 11(b).

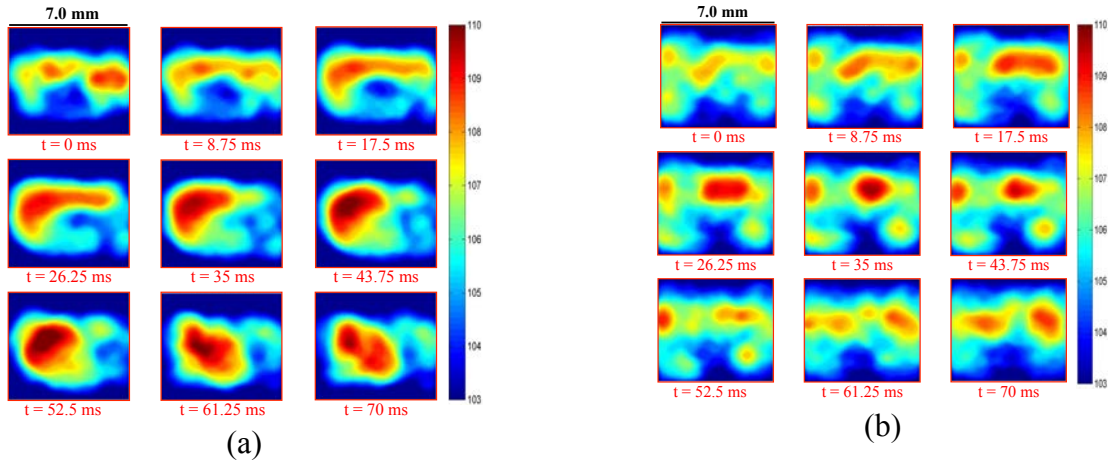


Figure 12. Local wall temperature distribution at $q''_h = 62.6 \text{ kW/m}^2$ in: (a) Case I, no ACEW and (b) Case II: ACEW-enhanced boiling ($V_{RMS} = 78 \text{ V}$, $f = 10 \text{ Hz}$). (Unit of the scale bar: $^\circ\text{C}$)

Based on the wall temperature measurement, the local heat flux is computed using the energy balance method. Figure 13 shows that although the thin-film heater provides uniform heating to the test piece, the heat flux on the boiling surface is not uniformly distributed owing to different pathways thermal energy takes to enter the bulk liquid. In the images, the contact line regions can be discerned by the bright-colored ring shapes where the heat flux values are higher. In contrast, the low-flux regions (marked by blue colors) correspond to the dry vapor patches underneath the bubbles as well as the regions in direct contact with the bulk liquid. Comparison of Figs. 13(a) and 13(b) manifests that ACEW leads to a larger surface area ratio of bright-colored, high-flux regions.

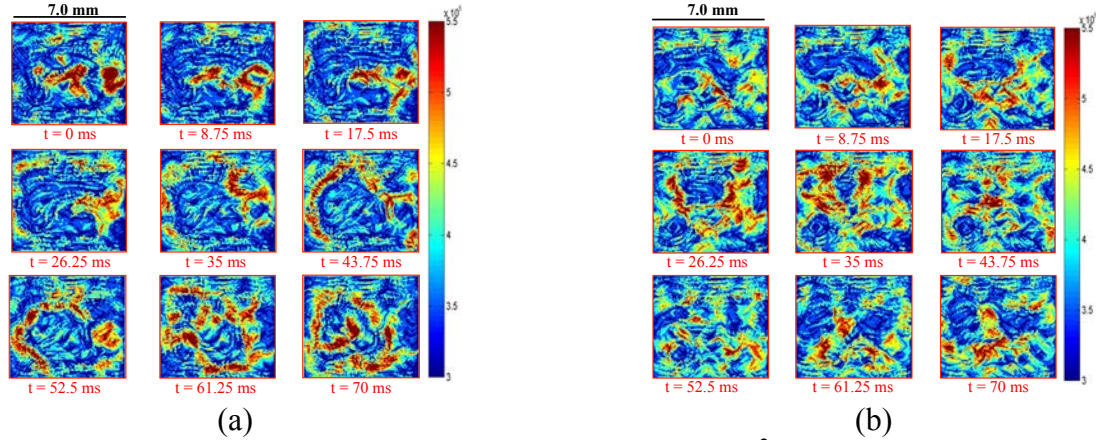


Figure 13. Local wall heat flux distribution at $q''_h = 62.6 \text{ kW/m}^2$ in: (a) Case I, no ACEW and (b) Case II: ACEW-enhanced boiling ($V_{RMS} = 78 \text{ V}$, $f = 10 \text{ Hz}$). (Unit of the scale bar: W/m^2)

To better comprehend ACEW-enhanced nucleate boiling, it is useful to examine the thermal energy transport processes on a hydrophilic surface and a hydrophobic surface. As schematically shown in Fig. 14(a), the primary boiling heat transfer mechanisms on a hydrophilic surface comprise of evaporation at the liquid-vapor interface of the bubble (especially from the meniscus of the microlayer), transient conduction in the surrounding liquid that flushes in to fill the void occupied by the bubble upon its departure, as well as microconvection in the wake of the departing bubble. In the case of nucleate boiling on a hydrophobic surface, Fig. 14(b) depicts that the liquid microlayer is absent due to the geometrical restriction imposed by the obtuse contact angle of the bubble. Thus, thermal energy is transferred through transient conduction, evaporation at the bubble surface, and microconvection [98, 99]. When ACEW is activated on the hydrophobic surface (Fig. 14(c)), the accelerated bubble ebullition greatly increases the rate at which the bulk liquid rewets the dryout areas on the surface, thereby improving the transient conduction heat transfer. In the meanwhile, the suppression of bubble coalescence results in a higher number density of bubbles per unit surface area, which promotes evaporation near the contact line, as indicated by the enlarged high-flux regions in Fig. 13(b). Moreover, although not directly measured in the present experiments, strong streaming flow has been observed in the proximate liquid of a bubble owing to ACEW-induced interfacial oscillations [71]. It is expected that the streaming flow will enhance liquid mixing near the wall and, thus, supplement the microconvection heat transfer.

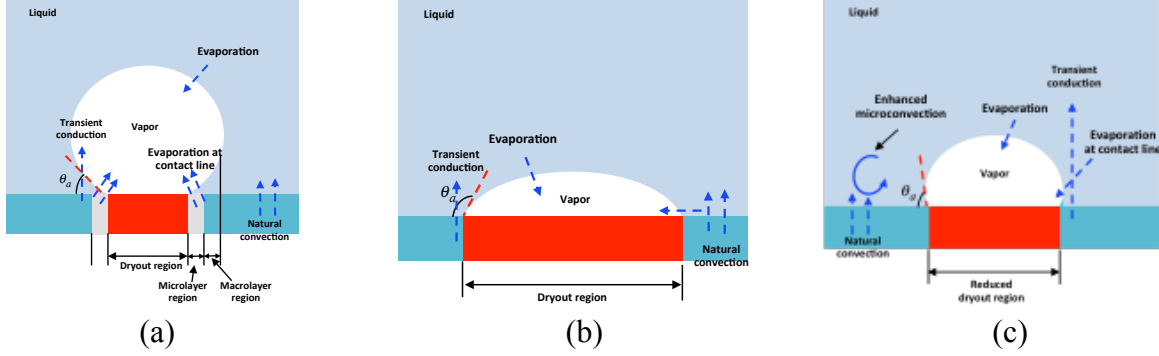


Figure 14. Primary heat transfer mechanisms during a bubble ebullition cycle on: (a) Hydrophilic surface, (b) Hydrophobic surface and (c) ACEW-enhanced surface.

4.3. Film boiling and CHF

At CHF, immense coalescence of bubbles causes the boiling surface to be blanketed by a thin vapor film. As a consequence, the bulk liquid is unable to reach the surface, i.e., the dryout occurs. In this work, the CHF condition is observed to take place at $q_h'' = 75.9 \text{ kW/m}^2$ on the hydrophobic surface (Case I). From Fig. 15(a), it is seen that a vapor film persists on the wall that feeds a big hovering bubble via a vapor column till it breaks off. In contrast, Fig. 15(b) shows that with ACEW, multiple individual bubbles, instead of a continuous vapor film, are found on the boiling surface at the same heat flux level ($q_h'' = 75.9 \text{ kW/m}^2$). The nucleation, growth and departure of each bubble can be clearly distinguished. Therefore, visually, ACEW reverts the film boiling regime in Fig. 15(a) to fully developed nucleate boiling in Fig. 15(b).

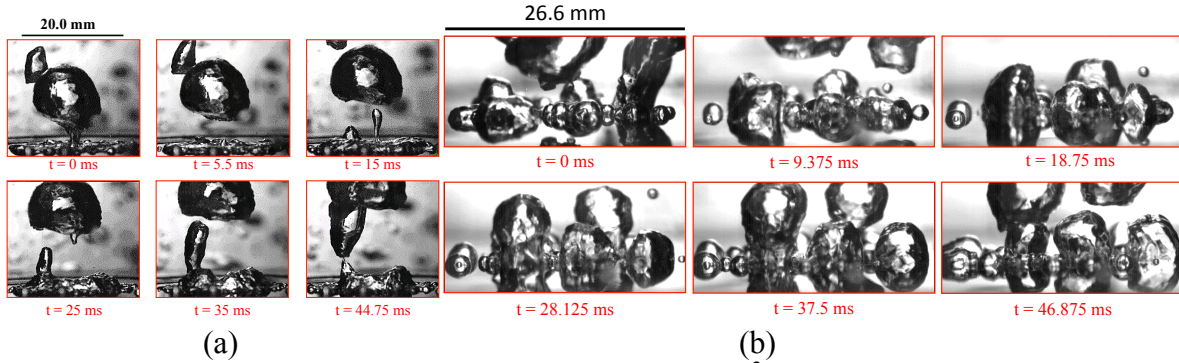


Figure 15. Filmwise transition boiling at $q_h'' = 75.9 \text{ kW/m}^2$ in: (a) Case I, no ACEW and (b) Case II: ACEW-enhanced boiling ($V_{RMS} = 78 \text{ V}$, $f = 10 \text{ Hz}$).

Figure 16(a) illustrates the instantaneous wall temperature distributions at CHF in Case I. Due to the insulating effect of the vapor film, the entire heated area of the boiling surface is occupied by a big hot spot ($140^\circ\text{C} \sim 205^\circ\text{C}$) with the peak temperature exceeding the Leidenfrost point [100]. This is marked as the burnout crisis as long time exposure of the surface to this high-temperature condition will cause the Teflon coating to peel off from the silicon substrate. When EW is actuated, the big hot spot disappears and, rather, some dispersed small hot spots are observed on the wall (Fig. 16(b)). It suggests the vapor film has disintegrated into discrete

nucleate bubbles, which is consistent with the visualization in Fig. 15(b). Furthermore, the maximum wall temperature reduces drastically to 110°C although the heat flux remains at the same level, owing to more effective heat transfer in fully developed nucleate boiling regime.

The heat transfer enhancement by ACEW is corroborated by the local heat flux distributions as shown in Fig. 17. Clearly, the low-heat-flux region in Case I (Fig. 17(a)), which represents the surface underneath the vapor film, is replaced by multiple smaller patches in Case II (Fig. 17(b)). Each patch is surrounded by a high-flux ring, an indicator of the contact line region around an individual bubble. Thus, ACEW helps to increase the contact line density (the contact line length per unit area) and the wetted area fraction (the fraction of the surface covered by liquid) on the boiling surface. Both factors contribute to the enhancement in CHF [95]. The subsequent experiments show the burnout crisis eventually occurs in Case II when the heat flux is increased to $q_h'' = 142.6 \text{ kW/m}^2$, i.e., an 87.9% increment in CHF compared to Case I without ACEW.

Based on the visual observations in Fig. 15, two questions must be answered in order to elucidate the role of ACEW played in the CHF process: (1) Why does the vapor film in Fig. 15(a) cease to exist in the presence of an electric field? (2) How can the bubbles in Fig. 15(b) avoid coalescing and spreading on the wall to form the vapor film even when they are subject to the CHF conditions? The first question can be addressed by exploring the similarity between the interfacial instabilities in film boiling at CHF and a Leidenfrost drop hovering over a highly superheated surface. For the Leidenfrost drop, the rapid vaporization of liquid from the side of the drop facing the surface produces a vapor layer that levitates the drop above the surface. If an electric field is applied between the drop and the solid substrate, a concentrated interfacial electric field will be induced across the vapor layer, leading to an electrostatic attraction force that disrupts the liquid-vapor interface and pulls the drop downward to rewet the surface, i.e., the Leidenfrost state is suppressed [101, 102]. In this study, the applied electric field is confined predominantly in the SiO₂ layer of the silicon wafer for an intimate liquid-solid contact or when the bubble size is large. However, when CHF occurs, the electric field will be biased toward the thin vapor film, due to its comparable electrical capacitance to the SiO₂ layer. When an AC field is actuated, it stimulates an oscillatory Maxwell stress force at the liquid-vapor interface, which will promote the hydrodynamic instability and cause the vapor film to collapse prematurely². This effect will persist till the wall superheat increases to such an extent that the vapor film will grow explosively to a thickness much larger than the SiO₂ layer immediately upon the liquid-solid contact, which sets the limit for ACEW-enhancement of CHF. The second question, the longevity of individual bubbles at CHF, can be understood by inspecting the force balance on a growing bubble. According to [103-105], CHF occurs when the vapor recoil force (i.e., a force resulting from the change of fluid momentum as the vapor phase leaves the liquid-vapor interface due to evaporation) overcomes the sum of the surface tension and gravitational forces that hold the bubble on the boiling surface. When ACEW is applied, it can be shown that the electrical force acts against the recoil force and is able to impede the spreading of the contact line on the boiling surface, thus delaying the occurrence of CHF [106].

² A DC field works much less effectively due to the lack of the dynamic destabilizing effect.

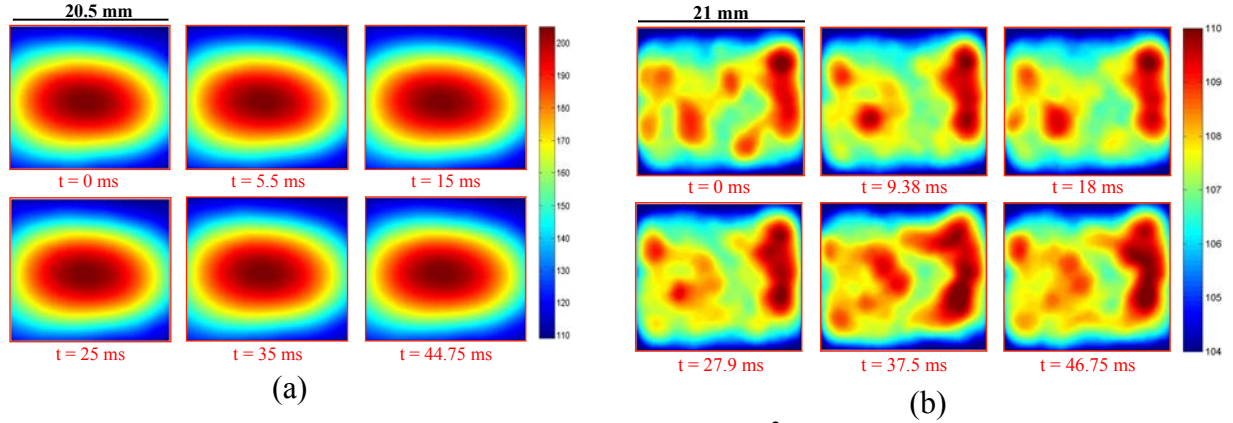


Figure 16. Wall temperature distribution at $q''_h = 75.9 \text{ kW/m}^2$ in: (a) Case I, no ACEW and (b) Case II: ACEW-enhanced boiling ($V_{RMS} = 78 \text{ V}$, $f = 10 \text{ Hz}$). (Unit of the scale bar: $^{\circ}\text{C}$)

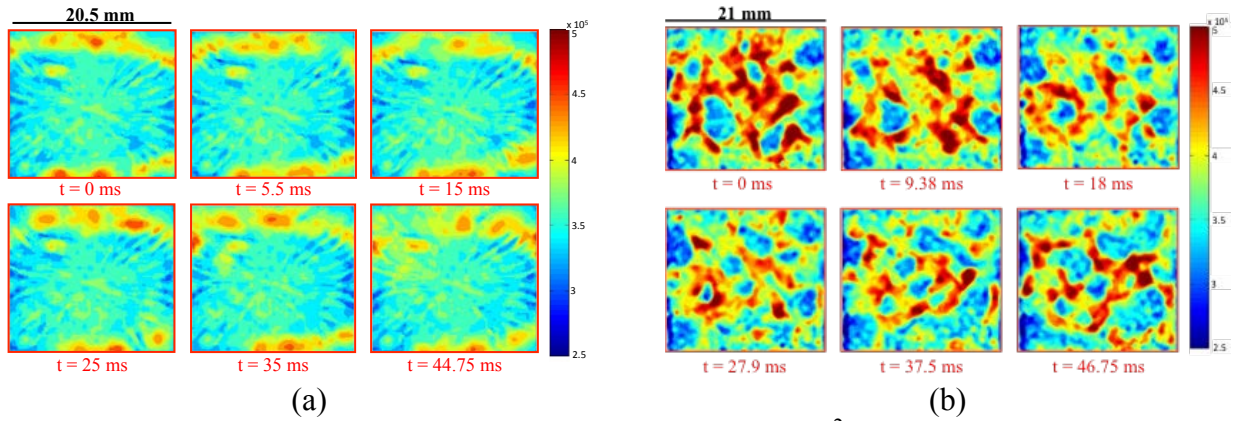


Figure 17. Local wall heat flux distribution at $q''_h = 75.9 \text{ kW/m}^2$ in: (a) Case I, no ACEW and (b) Case II: ACEW-enhanced boiling ($V_{RMS} = 78 \text{ V}$, $f = 10 \text{ Hz}$). (Unit of the scale bar: W/m^2)

4.4. Overall boiling heat transfer performance

In the foregoing sections, it has been demonstrated that ACEW effectively modulates the bubble dynamics and heat transfer characteristics in various boiling regimes. The effect of ACEW on the overall boiling heat transfer performance can be further appreciated from the boiling curve and the BHTC plot in Fig. 18, where the circular symbols represent Case I and the square symbols represent Case II.

Figure 18(a) depicts that the two boiling curves are almost indistinguishable at low heat fluxes when there is only liquid phase or very few sparse vapor bubbles residing on the surface. Once the heat flux is increased to $q''_h \sim 40 \text{ kW/m}^2$, the boiling curves start to diverge. Clearly, the ACEW effect causes the boiling curve to shift leftward with a steeper slope, which corresponds to the higher BHTC in Fig. 18(b). The boiling curve for the hydrophobic surface reaches a plateau at $q''_h = 75.9 \text{ kW/m}^2$, beyond which a slight increase in heat flux leads to a drastic jump in the wall superheat from 18°C to 35°C , i.e., the CHF condition is reached. By

comparison, the uprising trend of the ACEW-enhanced boiling curve continues to a much higher heat flux level ($q_h'' = 142.6 \text{ kW/m}^2$) till CHF eventually takes place. In accordance, Fig. 18(b) confirms that the maximum BHTC increases from $5.5 \text{ kW/m}^2\text{K}$ in Case I to $8.7 \text{ kW/m}^2\text{K}$ in Case II, representing a 41% improvement in boiling heat transfer.

It is worth noting that the mechanism of ACEW-induced enhancement of boiling heat transfer is fundamentally different from that of electrohydrodynamic (EHD) enhancement, although both originate from the applied electric field. The impact of EHD on bubble dynamics and general two-phase flow is primarily via the interfacial stress at the liquid-vapor interface produced by the electric field in the bulk fluid [107-110]. Thus, high voltage levels (\sim tens of kilovolts) are often needed to ensure sufficient EHD forces can be generated. In contrast, the electric field in EW is concentrated near the thin dielectric layer on the heated wall and the EW force acts only on the contact line, thereby requiring much lower actuation voltage.

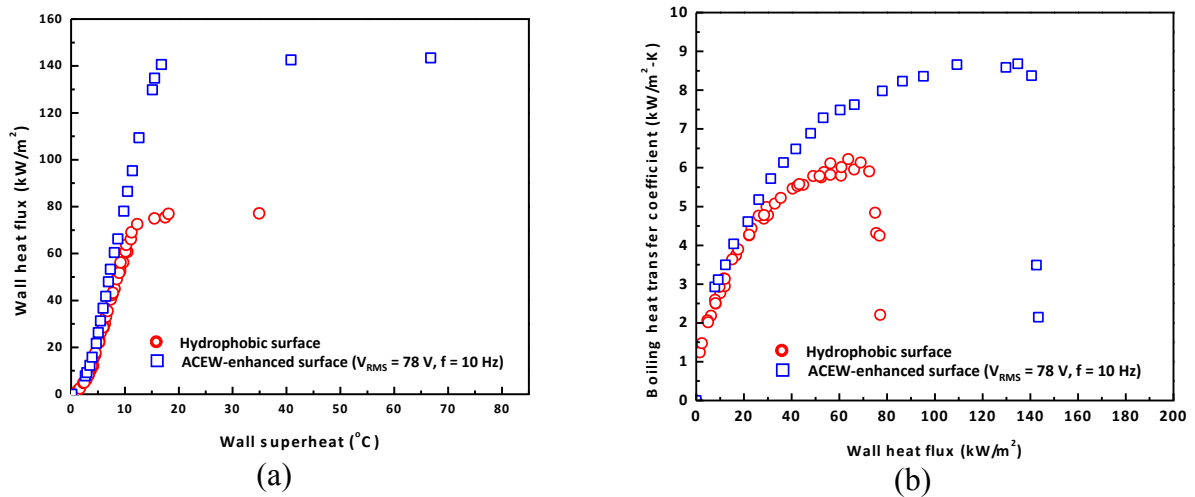


Figure 18. Comparison of pool boiling heat transfer performance: (a) boiling curve and (b) boiling heat transfer coefficient.

5. CONCLUSIONS

This work demonstrates that ACEW can be utilized to effectively enhance pool boiling heat transfer. The key impacts of ACEW on bubble dynamics include: 1) it constrains the spreading of the three-phase contact line on the boiling surface, and 2) it stimulates interfacial oscillations at the liquid-vapor interface and, subsequently, induces strong streaming flow in the liquid near the bubble. As a result, ACEW accelerates the ebullition cycle by triggering early bubble departure at ONB and suppresses bubble coalescence in fully developed nucleate boiling. Moreover, ACEW is able to destabilize the vapor film at CHF conditions and revert film boiling to nucleate boiling. It is observed that ACEW-enhanced pool boiling outperforms that on the baseline hydrophobic surface over the entire range of boiling conditions from ONB to CHF. In particular, CHF is improved by 85% and the maximum BHTC by 41%. Future work will focus on studying the transient processes when ACEW signal is actuated abruptly during the course of

pool boiling and developing theoretical models to quantify the CHF enhancement mechanisms by ACEW.

ACKNOWLEDGEMENTS

The authors acknowledge the financial supports from University of Houston and from the National Science Foundation (Grants No. 1134119 and No. 1236606).

REFERENCES

- [1] V.P. Carey, *Liquid–Vapor Phase-Change Phenomena*, Hemisphere, Washington, 1992.
- [2] R.L. Webb, N.H. Kim, *Principle of Enhanced Heat Transfer*, Taylor Francis, New York, 1994.
- [3] R.L. Webb, The Evolution of Enhanced Surface Geometries for Nucleate Boiling, *Heat Transfer Engineering*, 2(3-4) (1981) 23.
- [4] B.J. Jones, J.P. McHale, S.V. Garimella, The Influence of Surface Roughness on Nucleate Pool Boiling Heat Transfer, *Journal of Heat Transfer*, 131(12) (2009) 121009-121009.
- [5] S.J. Thiagarajan, S. Narumanchi, R. Yang, Effect of flow rate and subcooling on spray heat transfer on microporous copper surfaces, *International Journal of Heat and Mass Transfer*, 69(0) (2014) 493-505.
- [6] L.-W. Fan, J.-Q. Li, L. Zhang, Z.-T. Yu, K.-F. Cen, Pool boiling heat transfer on a nanoscale roughness-enhanced superhydrophilic surface for accelerated quenching in water, *Applied Thermal Engineering*, 109 (2016) 630-639.
- [7] H.H. Son, G.H. Seo, U. Jeong, S.J. Kim, Capillary wicking effect of a Cr-sputtered superhydrophilic surface on enhancement of pool boiling critical heat flux, *International Journal of Heat and Mass Transfer*, 113 (2017) 115-128.
- [8] S.M. You, J.H. Kim, K.H. Kim, Effect of nanoparticles on critical heat flux of water in pool boiling heat transfer, *Applied Physics Letters*, 83(16) (2003) 3374-3376.
- [9] D.H. Min, G.S. Hwang, Y. Usta, O.N. Cora, M. Koc, M. Kaviani, 2-D and 3-D modulated porous coatings for enhanced pool boiling, *International Journal of Heat and Mass Transfer*, 52(11–12) (2009) 2607-2613.
- [10] E. Forrest, E. Williamson, J. Buongiorno, L.-W. Hu, M. Rubner, R. Cohen, Augmentation of nucleate boiling heat transfer and critical heat flux using nanoparticle thin-film coatings, *International Journal of Heat and Mass Transfer*, 53(1–3) (2010) 58-67.
- [11] H. Seo, J.H. Chu, S.-Y. Kwon, I.C. Bang, Pool boiling CHF of reduced graphene oxide, graphene, and SiC-coated surfaces under highly wettable FC-72, *International Journal of Heat and Mass Transfer*, 82(0) (2015) 490-502.
- [12] R. Bertossi, N. Caney, J.A. Gruss, O. Poncelet, Pool boiling enhancement using switchable polymers coating, *Applied Thermal Engineering*, 77(0) (2015) 121-126.
- [13] S. Sarangi, J.A. Weibel, S.V. Garimella, Effect of particle size on surface-coating enhancement of pool boiling heat transfer, *International Journal of Heat and Mass Transfer*, 81(0) (2015) 103-113.
- [14] S. Das, D.S. Kumar, S. Bhaumik, Experimental study of nucleate pool boiling heat transfer of water on silicon oxide nanoparticle coated copper heating surface, *Applied Thermal Engineering*, 96 (2016) 555-567.

- [15] M.M. Sarafraz, F. Hormozi, Experimental investigation on the pool boiling heat transfer to aqueous multi-walled carbon nanotube nanofluids on the micro-finned surfaces, *International Journal of Thermal Sciences*, 100 (2016) 255-266.
- [16] A. Jaikumar, S.G. Kandlikar, Ultra-high pool boiling performance and effect of channel width with selectively coated open microchannels, *International Journal of Heat and Mass Transfer*, 95 (2016) 795-805.
- [17] M. Karimzadehkhoei, M. Shojaeian, K. Şendur, M.P. Mengüç, A. Koşar, The effect of nanoparticle type and nanoparticle mass fraction on heat transfer enhancement in pool boiling, *International Journal of Heat and Mass Transfer*, 109 (2017) 157-166.
- [18] A. Jaikumar, S.G. Kandlikar, A. Gupta, Pool Boiling Enhancement through Graphene and Graphene Oxide Coatings, *Heat Transfer Engineering*, 38(14-15) (2017) 1274-1284.
- [19] A. Khalili Sadaghiani, A.R. Motezakker, A.V. Özpınar, G. Özaydın İnce, A. Koşar, Pool boiling heat transfer characteristics of inclined pHEMA-coated surfaces, *Journal of Heat Transfer*, 139(11) (2017).
- [20] S. Launay, A.G. Fedorov, Y. Joshi, A. Cao, P.M. Ajayan, Hybrid micro-nano structured thermal interfaces for pool boiling heat transfer enhancement, *Microelectron J*, 37(11) (2006) 1158-1164.
- [21] S. Li, R. Furberg, M.S. Toprak, B. Palm, M. Muhammed, Nature-Inspired Boiling Enhancement by Novel Nanostructured Macroporous Surfaces, *Advanced Functional Materials*, 18(15) (2008) 2215-2220.
- [22] C.H. Li, T. Li, P. Hodgins, C.N. Hunter, A.A. Voevodin, J.G. Jones, G.P. Peterson, Comparison study of liquid replenishing impacts on critical heat flux and heat transfer coefficient of nucleate pool boiling on multiscale modulated porous structures, *International Journal of Heat and Mass Transfer*, 54(15-16) (2011) 3146-3155.
- [23] J.A. Weibel, S.S. Kim, T.S. Fisher, S.V. Garimella, Carbon Nanotube Coatings for Enhanced Capillary-Fed Boiling from Porous Microstructures, *Nanoscale and Microscale Thermophysical Engineering*, 16(1) (2012) 1-17.
- [24] J.Y. Ho, K.C. Leong, C. Yang, Saturated pool boiling from carbon nanotube coated surfaces at different orientations, *International Journal of Heat and Mass Transfer*, 79(0) (2014) 893-904.
- [25] C.M. Patil, S.G. Kandlikar, Pool boiling enhancement through microporous coatings selectively electrodeposited on fin tops of open microchannels, *International Journal of Heat and Mass Transfer*, 79(0) (2014) 816-828.
- [26] D.E. Kim, D.I. Yu, D.W. Jerng, M.H. Kim, H.S. Ahn, Review of boiling heat transfer enhancement on micro/nanostructured surfaces, *Experimental Thermal and Fluid Science*, 66(0) (2015) 173-196.
- [27] M. Ray, S. Deb, S. Bhaumik, Pool boiling heat transfer of refrigerant R-134a on TiO₂ nano wire arrays surface, *Applied Thermal Engineering*, 107 (2016) 1294-1303.
- [28] Y. Tang, J. Zeng, S. Zhang, C. Chen, J. Chen, Effect of structural parameters on pool boiling heat transfer for porous interconnected microchannel nets, *International Journal of Heat and Mass Transfer*, 93 (2016) 906-917.
- [29] S. Das, B. Saha, S. Bhaumik, Experimental study of nucleate pool boiling heat transfer of water by surface functionalization with crystalline TiO₂ nanostructure, *Applied Thermal Engineering*, 113 (2017) 1345-1357.

- [30] M. Zupančič, M. Može, P. Gregorčič, I. Golobič, Nanosecond laser texturing of uniformly and non-uniformly wettable micro structured metal surfaces for enhanced boiling heat transfer, *Applied Surface Science*, 399 (2017) 480-490.
- [31] P.A. Raghupathi, S.G. Kandlikar, Pool boiling enhancement through contact line augmentation, *Applied Physics Letters*, 110(20) (2017) 204101.
- [32] H.S. Jo, S. An, H.G. Park, M.-W. Kim, S.S. Al-Deyab, S.C. James, J. Choi, S.S. Yoon, Enhancement of critical heat flux and superheat through controlled wettability of cuprous-oxide fractal-like nanotextured surfaces in pool boiling, *International Journal of Heat and Mass Transfer*, 107 (2017) 105-111.
- [33] H.J. Cho, D.J. Preston, Y. Zhu, E.N. Wang, Nanoengineered materials for liquid–vapour phase-change heat transfer, *Nature Reviews Materials*, 2 (2016) 16092.
- [34] H.T. Phan, N. Caney, P. Marty, S. Colasson, J. Gavillet, Surface wettability control by nanocoating: The effects on pool boiling heat transfer and nucleation mechanism, *International Journal of Heat and Mass Transfer*, 52(23–24) (2009) 5459-5471.
- [35] H. Jo, M. Kaviani, S.H. Kim, M.H. Kim, Heterogeneous bubble nucleation on ideally-smooth horizontal heated surface, *International Journal of Heat and Mass Transfer*, 71(0) (2014) 149-157.
- [36] B. Bourdon, E. Bertrand, P. Di Marco, M. Marengo, R. Rioboo, J. De Coninck, Wettability influence on the onset temperature of pool boiling: Experimental evidence onto ultra-smooth surfaces, *Advances in Colloid and Interface Science*, 221(0) (2015) 34-40.
- [37] F. Villa, A. Georgoulas, M. Marengo, P. Di Marco, J. De Coninck, Pool Boiling Versus Surface Wettability Characteristics, (2016).
- [38] J. Kim, S. Jun, J. Lee, S.H. Lee, S.M. You, Effect of Wettability on Pool Boiling Incipience in Saturated Water, *Journal of Heat Transfer*, 138(8) (2016) 080910.
- [39] T. Harada, H. Nagakura, T. Okawa, Dependence of bubble behavior in subcooled boiling on surface wettability, *Nuclear Engineering and Design*, 240(12) (2010) 3949-3955.
- [40] Y. Nam, E. Aktinol, V.K. Dhir, Y.S. Ju, Single bubble dynamics on a superhydrophilic surface with artificial nucleation sites, *International Journal of Heat and Mass Transfer*, 54(7–8) (2011) 1572-1577.
- [41] X. Chen, H. Qiu, Bubble dynamics and heat transfer on a wettability patterned surface, *International Journal of Heat and Mass Transfer*, 88(0) (2015) 544-551.
- [42] M.T. Taylor, T. Qian, Thermal singularity and contact line motion in pool boiling: Effects of substrate wettability, *Physical Review E*, 93(3) (2016) 033105.
- [43] C. Marcel, A. Clausse, C. Frankiewicz, A. Betz, D. Attinger, Numerical investigation into the effect of surface wettability in pool boiling heat transfer with a stochastic-automata model, *International Journal of Heat and Mass Transfer*, 111 (2017) 657-665.
- [44] E. Teodori, T. Valente, I. Malavasi, A.S. Moita, M. Marengo, A.L.N. Moreira, Effect of extreme wetting scenarios on pool boiling conditions, *Applied Thermal Engineering*, 115(Supplement C) (2017) 1424-1437.
- [45] S.J. Kim, I.C. Bang, J. Buongiorno, L.W. Hu, Surface wettability change during pool boiling of nanofluids and its effect on critical heat flux, *International Journal of Heat and Mass Transfer*, 50(19–20) (2007) 4105-4116.
- [46] C.-C. Hsu, P.-H. Chen, Surface wettability effects on critical heat flux of boiling heat transfer using nanoparticle coatings, *International Journal of Heat and Mass Transfer*, 55(13–14) (2012) 3713-3719.

- [47] H.T. Phan, R. Bertossi, N. Caney, P. Marty, S. Colasson, A model to predict the effect of surface wettability on critical heat flux, *International Communications in Heat and Mass Transfer*, 39(10) (2012) 1500-1504.
- [48] S. Mori, S. Mt Aznam, K. Okuyama, Enhancement of the critical heat flux in saturated pool boiling of water by nanoparticle-coating and a honeycomb porous plate, *International Journal of Heat and Mass Transfer*, 80(0) (2015) 1-6.
- [49] S. Mori, Y. Utaka, Critical heat flux enhancement by surface modification in a saturated pool boiling: A review, *International Journal of Heat and Mass Transfer*, 108 (2017) 2534-2557.
- [50] N.a.C. Nagai, V.P., Assessment of Surface Wettability and Its Relation to Boiling Phenomena, *Thermal Science and Engineering*, 10(3) (2002) 10.
- [51] C.-H. Choi, M. David, Z. Gao, A. Chang, M. Allen, H. Wang, C.-h. Chang, Large-scale Generation of Patterned Bubble Arrays on Printed Bi-functional Boiling Surfaces, *Scientific Reports*, 6 (2016) 23760.
- [52] Y. Takata, Hidaka, S. Kohno, M, Enhanced nucleate boiling by superhydrophobic coating with checkered and spotted patterns, in: *International Conference on Boiling Heat Transfer*, Spoleto, 2006.
- [53] A.R. Betz, J. Xu, H.H. Qiu, D. Attinger, Do surfaces with mixed hydrophilic and hydrophobic areas enhance pool boiling?, *Applied Physics Letters*, 97(14) (2010).
- [54] H. Jo, H.S. Ahn, S. Kang, M.H. Kim, A study of nucleate boiling heat transfer on hydrophilic, hydrophobic and heterogeneous wetting surfaces, *International Journal of Heat and Mass Transfer*, 54(25–26) (2011) 5643-5652.
- [55] A.R. Betz, J. Jenkins, C.J. Kim, D. Attinger, Boiling heat transfer on superhydrophilic, superhydrophobic, and superbiphilic surfaces, *International Journal of Heat and Mass Transfer*, 57(2) (2013) 733-741.
- [56] H. Jo, S. Kim, H.S. Park, M.H. Kim, Critical heat flux and nucleate boiling on several heterogeneous wetting surfaces: Controlled hydrophobic patterns on a hydrophilic substrate, *International Journal of Multiphase Flow*, 62(0) (2014) 101-109.
- [57] H. Jo, D.I. Yu, H. Noh, H.S. Park, M.H. Kim, Boiling on spatially controlled heterogeneous surfaces: Wettability patterns on microstructures, *Applied Physics Letters*, 106(18) (2015).
- [58] A. Fazeli, M. Mortazavi, S. Moghaddam, Hierarchical biphilic micro/nanostructures for a new generation phase-change heat sink, *Applied Thermal Engineering*, 78 (2015) 380-386.
- [59] M. Zupančič, M. Steinbücher, P. Gregorčič, I. Golobič, Enhanced pool-boiling heat transfer on laser-made hydrophobic/superhydrophilic polydimethylsiloxane-silica patterned surfaces, *Applied Thermal Engineering*, 91 (2015) 288-297.
- [60] R. Holguin, K. Kota, S. Wootton, R.-H. Chen, S. Ross, Enhanced boiling heat transfer on binary surfaces, *International Journal of Heat and Mass Transfer*, 114 (2017) 1105-1113.
- [61] X. Dai, X. Huang, F. Yang, X. Li, J. Sightler, Y. Yang, C. Li, Enhanced nucleate boiling on horizontal hydrophobic-hydrophilic carbon nanotube coatings, *Applied Physics Letters*, 102(16) (2013) 161605.
- [62] A.S. Kousalya, K.P. Singh, T.S. Fisher, Heterogeneous wetting surfaces with graphitic petal-decorated carbon nanotubes for enhanced flow boiling, *International Journal of Heat and Mass Transfer*, 87(0) (2015) 380-389.
- [63] H. Jo, D.I. Yu, H. Noh, H.S. Park, M.H. Kim, Boiling on spatially controlled heterogeneous surfaces: Wettability patterns on microstructures, *Applied Physics Letters*, 106(18) (2015) 181602.

- [64] C.S.S. Kumar, Y.W. Chang, P.-H. Chen, Effect of heterogeneous wettable structures on pool boiling performance of cylindrical copper surfaces, *Applied Thermal Engineering*, (2017).
- [65] R. Wen, Q. Li, W. Wang, B. Latour, C.H. Li, C. Li, Y.-C. Lee, R. Yang, Enhanced Bubble Nucleation and Liquid Rewetting for Highly Efficient Boiling Heat Transfer on Two-Level Hierarchical Surfaces with Patterned Copper Nanowire Arrays, *Nano Energy*, (2017).
- [66] Y. Takata, S. Hidaka, J.M. Cao, T. Nakamura, H. Yamamoto, M. Masuda, T. Ito, Effect of surface wettability on boiling and evaporation, *Energy*, 30(2–4) (2005) 209-220.
- [67] B.J. Zhang, R. Ganguly, K.J. Kim, C.Y. Lee, Control of pool boiling heat transfer through photo-induced wettability change of titania nanotube arrayed surface, *International Communications in Heat and Mass Transfer*, 81 (2017) 124-130.
- [68] A.S. Kousalya, C.N. Hunter, S.A. Putnam, T. Miller, T.S. Fisher, Photonically enhanced flow boiling in a channel coated with carbon nanotubes, *Applied Physics Letters*, 100(7) (2012) 071601.
- [69] C.N. Hunter, D.B. Turner, M.L. Jespersen, M.H. Check, P.T. Borton, N.R. Glavin, A.A. Voevodin, Fast photo-switchable surfaces for boiling heat transfer applications, *Applied Physics Letters*, 101(19) (2012) 191603.
- [70] H.J. Cho, J.P. Mizerak, E.N. Wang, Turning bubbles on and off during boiling using charged surfactants, *Nature Communications*, 6 (2015) 8599.
- [71] S.H. Ko, Lee, S. J., and Kang, K. H., A synthetic jet produced by electrowetting-driven bubble oscillations in aqueous solution, *Applied Physics Letters*, 94(19) (2009) 194102.
- [72] T.D. Blake, A. Clarke, E.H. Stattersfield, An Investigation of Electrostatic Assist in Dynamic Wetting, *Langmuir*, 16(6) (2000) 2928-2935.
- [73] J. Lahann, S. Mitragotri, T.-N. Tran, H. Kaido, J. Sundaram, I.S. Choi, S. Hoffer, G.A. Somorjai, R. Langer, A Reversibly Switching Surface, *Science*, 299(5605) (2003) 371-374.
- [74] N. Verplanck, Y. Coffinier, V. Thomy, R. Boukherroub, Wettability Switching Techniques on Superhydrophobic Surfaces, *Nanoscale Res Lett*, 2(12) (2007) 577-596.
- [75] N. Mori, H. Horikawa, H. Furukawa, T. Watanabe, Temperature-Induced Changes in the Surface Wettability of SBR + PNIPA Films, *Macromolecular Materials and Engineering*, 292(8) (2007) 917-922.
- [76] D. Wang, X. Wang, X. Liu, F. Zhou, Engineering a Titanium Surface with Controllable Oleophobicity and Switchable Oil Adhesion, *The Journal of Physical Chemistry C*, 114(21) (2010) 9938-9944.
- [77] F. Mugele, J.C. Baret, Electrowetting: From basics to applications, *J Phys-Condens Mat*, 17(28) (2005) R705-R774.
- [78] J. Atencia, D.J. Beebe, Controlled microfluidic interfaces, *Nature*, 437(7059) (2005) 648-655.
- [79] H.L. Bralower, A study of electrowetting-assisted boiling, (2011).
- [80] J. Hong, S. Ko, K. Kang, I. Kang, A numerical investigation on AC electrowetting of a droplet, *Microfluid Nanofluid*, 5(2) (2008) 263-271.
- [81] L. Chen, E. Bonaccorso, Electrowetting — From statics to dynamics, *Advances in Colloid and Interface Science*, 210 (2014) 2-12.
- [82] J.M. Oh, S.H. Ko, K.H. Kang, Shape Oscillation of a Drop in ac Electrowetting, *Langmuir*, 24(15) (2008) 8379-8386.

- [83] Y. Lu, Sur, A., Tang, Y., Carmen, P., Annapragada, Ruthhoeft, P., Liu, D., Dynamics of droplet motion induced by electrowetting International Journal of Heat and Mass Transfer, 106 (2017) 920-931.
- [84] S. Chung, K. Rhee, S. Cho, Bubble actuation by electrowetting-on-dielectric (EWOD) and its applications: A review, Int. J. Precis. Eng. Manuf., 11(6) (2010) 991-1006.
- [85] A. Sur, An experimental investigation of electrowetting modulated nucleate boiling, University of Houston, Houston, TX, 2014.
- [86] C. Gerardi, J. Buongiorno, L.-w. Hu, T. McKrell, Study of bubble growth in water pool boiling through synchronized, infrared thermometry and high-speed video, International Journal of Heat and Mass Transfer, 53(19–20) (2010) 4185-4192.
- [87] W. Kaiser, H.Y. Fan, Infrared Absorption of Indium Antimonide, Phys Rev, 98(4) (1955) 966-968.
- [88] T.S. Moss, T.D.H. Hawkins, The Infra-Red Emissivities of Indium Antimonide and Germanium, P Phys Soc Lond, 72(464) (1958) 270-273.
- [89] Gerritsm.Cj, J.H. Haanstra, Infrared Transmission of Air under Laboratory Conditions, Infrared Phys, 10(2) (1970) 79-90.
- [90] M.H.N. Naraghi, V.W. Antonetti, Macro-constriction resistance of distributed contact contour areas in a vacuum environment, in: A. HTD (Ed.) ASME Winter Annual Meeting, 1993, pp. 107-114.
- [91] S. Lee, S. Song, V. AU, K.P. Moran, Constriction/spreading resistance model for electronics packaging, in: ASME (Ed.) ASME/JSME Thermal Engineering Conference, 1995.
- [92] E. Wagner, P. Stephan, High-Resolution Measurements at Nucleate Boiling of Pure FC-84 and FC-3284 and Its Binary Mixtures, J Heat Trans-T Asme, 131(12) (2009).
- [93] Y. Heng, A. Mhamdi, E. Wagner, P. Stephan, W. Marquardt, Estimation of local nucleate boiling heat flux using a three-dimensional transient heat conduction model, Inverse Probl Sci En, 18(2) (2010) 279-294.
- [94] S. Jung, H. Kim, Synchronized measurement of liquid-vapor phase and temperature distributions on a boiling surface during single bubble nucleate boiling, in: 8th International Conference on Multiphase Flow, Jeju, Korea, 2013.
- [95] J. Jung, S.J. Kim, J. Kim, Observations of the Critical Heat Flux Process During Pool Boiling of FC-72, Journal of Heat Transfer, 136(4) (2014) 041501-041501.
- [96] C.D. Gerardi, Investigation of pool boiling heat transfer enhancement of nano engineered fluids by means of high-speed infrared thermography, Dissertation, Massachusetts Institute of Technology, Boston, 2009.
- [97] S.J. Kline, I.A. McClintok, Describing uncertainties in single-sample experiments, Mechanical Engineering, (January) (1953) 3-8.
- [98] H.T. Phan, N. Caney, P. Marty, S. Colasson, J. Gavillet, A. Marechal, Influence of Surface Wettability on Pool Boiling Heat Transfer, Icnmm 2009, Pts a-B, (2009) 17-23.
- [99] H.T. Phan, N. Caney, P. Marty, S. Colasson, J. Gavillet, Effects of Surface Wettability on Heterogeneous Boiling, Mnhmt2009, Vol 2, (2010) 91-96.
- [100] L. Yi, Bao, J.M., and Liu, D., Dynamics of a Leidenfrost droplet modulated by electrowetting, Journal of Heat Transfer, in review. (2017).
- [101] F. Celestini, G. Kirstetter, Effect of an electric field on a Leidenfrost droplet, Soft Matter, 8(22) (2012) 5992-5995.

- [102] A. Shahriari, J. Wurz, V. Bahadur, Heat Transfer Enhancement Accompanying Leidenfrost State Suppression at Ultrahigh Temperatures, *Langmuir*, 30(40) (2014) 12074-12081.
- [103] K. Sefiane, D. Benielli, A. Steinchen, A new mechanism for pool boiling crisis, recoil instability and contact angle influence, *Colloids and Surfaces A: Physicochemical and Engineering Aspects*, 142(2–3) (1998) 361-373.
- [104] V.S. Nikolayev, D.A. Beysens, Boiling crisis and non-equilibrium drying transition, *EPL (Europhysics Letters)*, 47(3) (1999) 345.
- [105] S.G. Kandlikar, A Theoretical Model to Predict Pool Boiling CHF Incorporating Effects of Contact Angle and Orientation, *Journal of Heat Transfer*, 123(6) (2001) 1071-1079.
- [106] A. Sur, Lu, Y., Carmen, P., Ruthhoeft, P., Bao, J. M., Liu, D., Enhancing critical heat flux with electrowetting, in preparation., (2017).
- [107] J. Seyed-Yagoobi, J.E. Bryan, Enhancement of heat transfer and mass transport in single-phase and two-phase flows with electrohydrodynamics, *Advances in Heat Transfer*, 33 (1999) 95-186.
- [108] J.E. Bryan, J. Seyed-Yagoobi, Influence of flow regime, heat flux, and mass flux on electrohydrodynamically enhanced convective boiling, *Journal of Heat Transfer*, 123(2) (2001) 355-367.
- [109] V.K. Patel, J. Seyed-Yagoobi, Combined Dielectrophoretic and Electrohydrodynamic Conduction Pumping for Enhancement of Liquid Film Flow Boiling, *Journal of Heat Transfer*, 139(6) (2017) 061502.
- [110] V. Pandey, G. Biswas, A. Dalal, Saturated film boiling at various gravity levels under the influence of electrohydrodynamic forces, *Physics of Fluids*, 29(3) (2017) 032104.